Chinese Chemical Letters 34 (2023) 107502

Contents lists available at ScienceDirect

Chinese Chemical Letters

journal homepage: www.elsevier.com/locate/cclet

Colorimetric-assisted photoelectrochemical sensing for dual-model detection of sialic acid *via* oxidation-power mediator integration

Yuanyuan Cheng, Rong-Mei Kong, Wenao Hu, Xiaoxia Tian, Lingdong Zhang, Lian Xia*, Fengli Qu*

School of Chemistry and Chemical Engineering, Qufu Normal University, Qufu 273165, China

ARTICLE INFO

Article history:
Received 12 January 2022
Revised 21 April 2022
Accepted 8 May 2022
Available online 11 May 2022

Keyword:
Sialic acid
Photoelectrochemical sensor
Visualization
Metal organic frameworks
Dual-mode readout

ABSTRACT

Development of sensitive and accurate methods for sialic acid (SA) determination is of great significance in early cancer diagnosis. Here, a colorimetric-assisted Photoelectrochemical (PEC) sensor was constructed for SA detection based on the two pairs of *cis*-diol groups in SA molecule. With the specific recognition of SA *via* the two pairs of *cis*-diol groups, the prepared gold-modified Bi_2S_3 (Au NPs@Bi_2S_3) and metal organic framework (Au@PCN-224) were introduced to the electrode and formed a sandwich structure. Based on the properties of inert electroconductivity and nanozyme of the PCN-224, dual-readout of photocurrent and visualization was achieved with the presence of 3,3′,5,5′-tetramethylbenzidine (TMB). Moreover, to intensify the visualization signal, Ce^{3+} was employed as the mediator to boost the catalysis capability by transferring energy from PCN-224 surface to the whole system. With the unique SA recognition and the mediation of Ce^{3+}, both the photocurrent and the visualization signals sensitively responded with the SA concentration linearly. The present method showed greatly high sensitivity, selectivity and accuracy for SA detection with a limit of detection of 1.44 μmol/L and a wide linear range of 5–1000 μmol/L. This method provided a new promising platform for SA detection and a potential strategy for design of novel biosensors with dual-model readout.

Sialic acid (SA), a monosaccharide with 9-carbon backbone (C1–9), usually located at the outer end of glycans (sialoglycans), playing a vital physiological part in human body [1,2]. The prominent position on the cell surface enabled sialoglycans participate in intracellular and intercellular matrix interaction, such as adhesion, migration, and immune recognition [3–5]. Previous studies showed that tumor cells from various origins, such as pancreatic cancer [6], breast cancer [7], colon cancer [8], cervical cancer [9], expressed increased amount of SA on surface sialoglycans and their secretion into tumor microenvironment. As a result, aberrant expression of SA in blood serum or cell membrane were implicated as an early stage of cancers [10]. Therefore, monitoring SA in serum or cell membrane during biological processes was of great importance for cancer diagnosis.

Various SA detection technologies, including mass spectrometry [11], high performance liquid chromatography [12], fluorescence spectrometry [13,14], colorimetric sensor [15], and electrochemical sensor [16] were sufficiently explored as promising approaches in recent years. Although those methods achieved satisfactory results, they still suffered some disadvantages. For example, mass spectrometry and chromatography methods required expensive instruments, together with complex sample pretreatment with a long analysis time; fluorescence and colorimetric methods were susceptible to interference and showed dissatisfactory sensitivity; electrochemical methods were plagued with high background signals and poor repeatability. Photoelectrochemical (PEC) biosensor, a new electrochemical analysis technology contributed by photoactive species, showed efficient photo-to-electric conversion ability under light irradiation [17,18]. Due to the separated excitation source (light) and detection signal (photocurrent), PEC immunoassay produced reduced background signals and showed characteristics of high sensitivity, low-cost instruments, high rate, and inherent miniaturization [19–22]. However, single-model pattern of PEC biosensors could be easily affected by external interferences, leading to uncertainty and even possibility of false positive results. To address these problems, colorimetric-assisted PEC sensors were proposed to improve the accuracy of the PEC sensors [23,24]. Owing to the different mechanisms and separate signals between PEC and colorimetry, these two different modes of signal could not interfere each other even in one sensing system, therefore the results could be mutually verified with more accu-

* Corresponding authors.
E-mail addresses: xialian01@163.com (L. Xia), fengliquhn@hotmail.com (F. Qu).

https://doi.org/10.1016/j.cclet.2022.05.016
1001-8417/

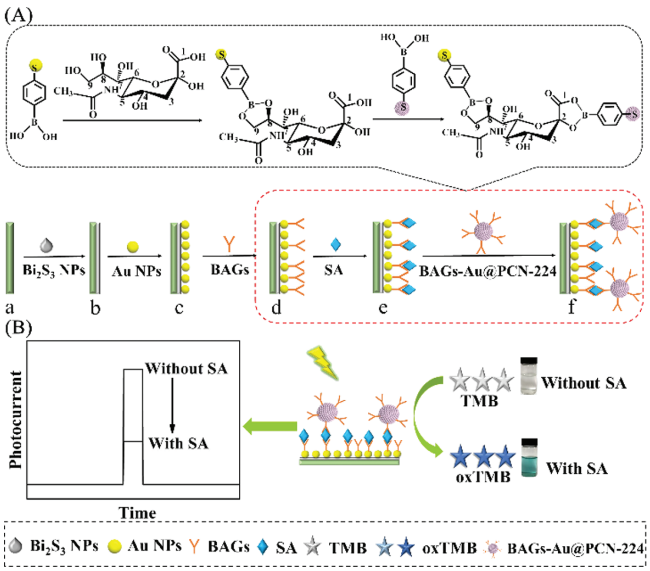

Scheme 1. (A) Schematic diagram showing the fabrication process of PEC biosensor for SA detection. (B) The dual-readout pattern of the colorimetric-assisted photoelectrochemical sensing.

racy. Benefiting from the advantages of nanozymes, construction of colorimetric-assisted PEC sensor using nanozymes with the presence of chromogenic substrates showed great attraction. Among various nanozymes, metal organic frameworks (MOFs) with porphyrins as ligands (PCN-224) not only exhibited unique characteristics of good crystallinity, high porosity, and large surface area but also had versatile functions in catalysis and light capture [25–28]. Especially, the PCN-224 showed the integrated properties of inert electroconductivity and nanozyme [29,30]. Here, we proposed that PCN-224 wondered a great potential in colorimetric-assisted PEC sensing.

In this study, a colorimetric-assisted PEC sensor was constructed for SA detection based on the two pairs of *cis*-diol groups in one SA molecule. Gold modified bismuth sulfide (Au NPs@Bi_2S_3) was synthesized and used to modify electrode to get initial high photocurrent. The prepared gold-modified PCN-224 (Au@PCN-224), a signal amplifier, was successfully introduced to the electrode *via* the specific recognition of SA assisted by boric acid and formed a sandwich structure (Scheme 1A). Owing to the properties of inert electroconductivity and nanozyme of the PCN-224, dual-mode readout of photocurrent and visualization was achieved with the presence of 3,3′,5,5′-tetramethylbenzidine (TMB). Moreover, to intensify the colorimetric signal, Ce^{3+} was employed as the mediator to boost the oxidation-power by transferring energy from PCN-224 surface to the whole system (Scheme 1B). Therefore, with the unique SA recognition and the mediation of Ce^{3+}, both the photocurrent and the visualization signals sensitively responded with the SA concentration linearly.

The photoelectric layer material played a crucial role in PEC biosensors. Due to the narrow band gap and high photoelectron conversion efficiency [31–34], Bi_2S_3 was selected as the light-harvesting substrate to modify indium-tin oxide (ITO) slice for development of working photoelectrode. In order to introduce boric acid groups (BAGs, specific groups to bond with SA) on the electrode surface in the next step [35–39], gold nanoparticles (Au NPs) were employed to functionalize Bi_2S_3 *via* the Au-S covalent bond (Au NPs@Bi_2S_3). Figs. 1A and B and Fig. S1 (Supporting information) showed the SEM and high-resolution TEM (HRTEM) images of the as-synthesized Bi_2S_3, revealing that the Bi_2S_3 was uniform nanoparticle with high crystal lattice. Moreover, it was noted that Bi_2S_3 was 5 nm in size (Fig. S2 in Supporting information). After Au NPs bonding with the Bi_2S_3, the resulted Au NPs@Bi_2S_3 showed dispersive and uniform decoration with Au NPs (Fig. 1C). To confirm the successful preparation of the BAGs functionalized Au NPs@Bi_2S_3 (BAGs-Au NPs@Bi_2S_3), the energy-dispersive spectrometry (EDS) mapping was carried out and the results were shown in Figs. 1D and E and Table S1 (Supporting information). The Au, Bi, S and B elements were uniformly distributed in the hybrid material. UV–vis adsorption was used to evaluate the optical property of the Au NPs@Bi_2S_3. As seen from Fig. 1F, Bi_2S_3 NPs exhibited an extensive absorption range with suitable adsorption intensity (black line) and Au NPs showed a characteristic adsorption peak at 520 nm (red line). The hybrid of Au NPs@Bi_2S_3 showed integrated adsorption of Bi_2S_3 NPs and Au NPs, ranging from 300 nm to 700 nm with a distinct adsorption peak at 520 nm (blue line), which could absorb near-infrared light. The Fourier transform-infrared (FT-IR) spectra of Bi_2S_3, Au@Bi_2S_3 and BAGs-Au@Bi_2S_3 were showed in Fig. S3A (Supporting information). No significant difference was observed on the characteristic FT-TR spectrum peaks between Bi_2S_3 and Au@Bi_2S_3, indicating the existence of Au did not affect the functional groups of the Bi_2S_3, and the peak located at 1012 cm^{-1} was ascribed to B-OH, indicating the successful synthesis of BAGs-Au@Bi_2S_3.

The morphology of the as-synthesized PCN-224 was first investigated by SEM (Fig. 2A) and TEM (Fig. S4 in Supporting information), which showed that the PCN-224 was uniform and had a regular spherical shape. After the PCN-224 combining with the Au NPs, the resulted Au@PCN-224 surface became obviously rough according to the SEM images (Fig. 2B), and the Au NPs were well decorated on the surface of PCN-224 (Fig. 2C). Fig. S5 (Supporting information) showed that the crystalline PCN-224 was size-uniform with the average diameter of about 100 nm, which highly consisted with the results of the SEM and TEM. The successful preparation of Au@PCN-224 was further confirmed by the powder X-ray diffraction (PXRD). From Fig. 2D, all the diffraction peaks of PCN-224 were well consistent with those reported by previous literatures [40]. After functionalized with Au NPs, the resulted Au@PCN-224 showed both PXRD patterns of Au and PCN-224, indicating that the Au@PCN-224 was successfully prepared and the Au NPs did not influence the crystallinity of the PCN-224. The FT-IR spectra of PCN-224, Au@PCN-224 and BAGs-Au@PCN-224 were showed in Fig. S3B. The peak located at 3451 and 1385 cm^{-1} were ascribed to the O–H stretching vibration. The peak located at 1685 cm^{-1} was ascribed to C = O bond. The unnoticeable peak located at 1012 cm^{-1} was ascribed to the B–O adsorption bonds and due to the relatively low content of B. The spectra result further confirmed the BAGs-Au@PCN-224 was successfully synthesized.

As shown in Fig. S6A (Supporting information), the PCN-224 had a porous structure, and the Brunauer-Emmett-Teller (BET) surface area and the total pore volume were 1367 m^2/g and 0.938 cm^3/g, respectively. After *in situ* generating Au NPs on the PCN-224 surface, the BET surface area of the resulting Au@PCN-224 was slightly declined due to the Au NPs occupying some cavities. Based on the high surface area and large pore volume, the porous Au@PCN-224 nanohybrid provided enough catalytic sites and facilitated the molecules transfer and ions diffusion. Moreover, UV–vis extinction spectra of the PCN-224 and Au@PCN-224 were shown in Fig. S6B (Supporting information). A shift of S- and Q-band of the PCN-224 were observed after the growth of Au NPs, demonstrating the successful combination of PCN-224 with Au NPs. The X-ray photoelectron spectroscopy (XPS) data (Figs. S6C and D in Supporting information) demonstrated that the Au NPs were combined with PCN-224 *via* Au-N bond between Au NPs and PCN-224. In addition, the successful preparation of the BAGs functionalized Au@PCN-224 (BAGs-Au@PCN-224) was confirmed by SEM image (Fig. S7 in Supporting information). From the Fig. S7, after be-

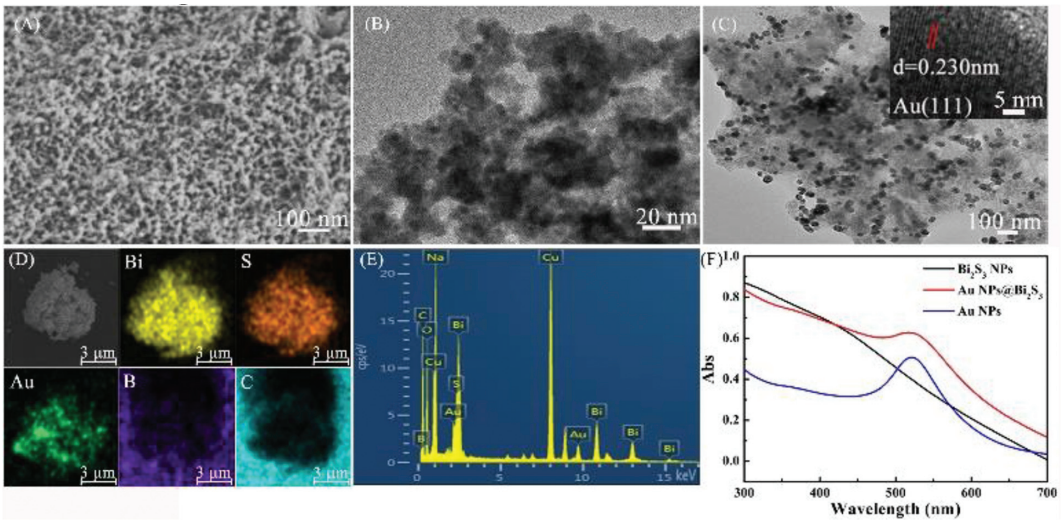

Fig. 1. (A) SEM and (B) HRTEM image of Bi_2S_3 NPs. (C) TEM image of Au NPs@Bi_2S_3. The inset plot is Au NPs. (D) Thermal field SEM image of BAGs-Au NPs@Bi_2S_3 and the elemental mappings for Bi, S, Au, B and C of BAGs-Au NPs@Bi_2S_3. (E) The TEM-EDS elemental analyses of BAGs-Au NPs@Bi_2S_3. (F) UV–vis absorption spectra of Bi_2S_3 NPs (black), Au NPs@Bi_2S_3 (red) and Au NPs (blue).

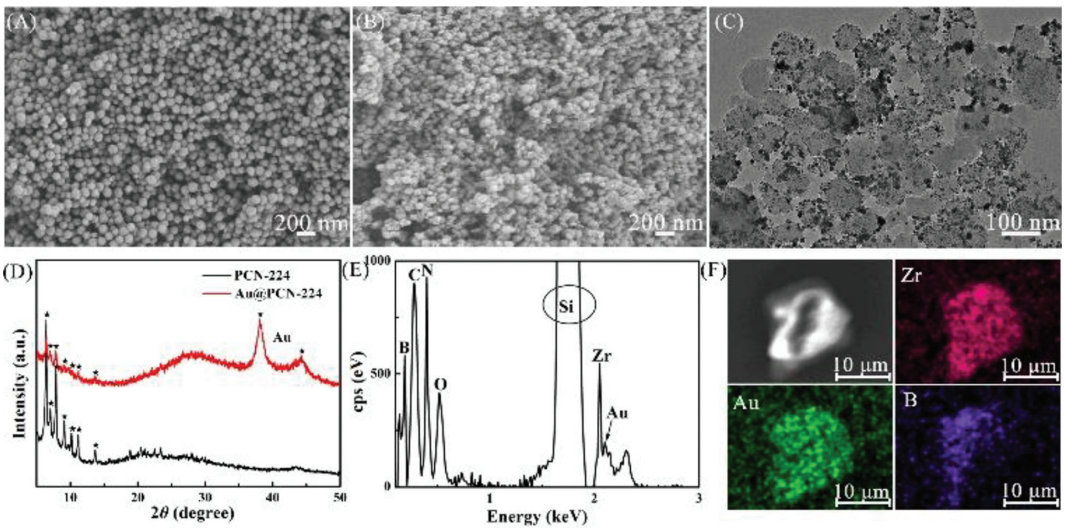

Fig. 2. (A) SEM image of PCN-224. (B) SEM and (C) TEM images of Au@PCN-224. (D) PXRD of synthetic PCN-224 (black) and Au@PCN-224 (red). (E) The SEM-EDS elemental analyses of BAGs-Au@PCN-224. (F) Thermal field SEM image and the elemental mappings for Zr, Au, and B of BAGs-Au@PCN-224.

ing functionalized with BAGs, the initial morphology of Au@PCN-224 was well retained, and the elements of Au and B could be clearly found through the element mapping map and the EDS data (Figs. 2E and F, and Table S2 in Supporting information). These results indicated that the BAGs-Au@PCN-224 was successfully synthesized as expected.

EIS was a powerful approach for evaluating the electron transfer behavior of different electrodes. Fig. 3A exhibited the Nyquist plots of each electrode for different modification steps, which reflected the charge-transfer resistance (R_{ct}) corresponding to semicircle diameters. According to Fig. 3A, the R_{ct} value of ITO was firstly determined to be 18.05 Ω (curve a), while after modification with Bi_2S_3 NPs, the Bi_2S_3/ITO electrode exhibited a significantly increased semicircle with a R_{ct} value of 40.17 Ω (curve b). However, when the Bi_2S_3/ITO was further immobilized with Au NPs, the R_{ct} of Au NPs/Bi_2S_3/ITO significantly decreased to be 21.30 Ω (curve c), due to the good conductivity, unique surface Plasmon resonance and wide adsorption spectra of the Au NPs [41,42]. Nevertheless, with continuing modification with BAGs, SA and BAGs-Au@PCN-224 in sequence, the R_{ct} of the resulted electrodes increased to be

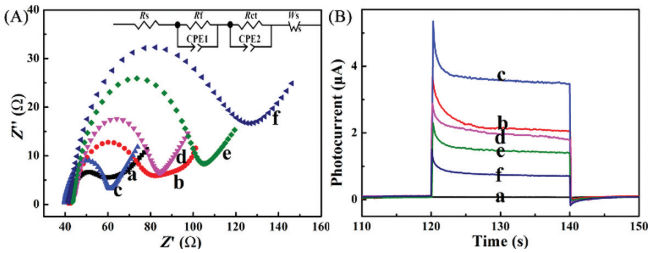

Fig. 3. (A) EIS responses of fabrication process: (a) ITO, (b) Bi_2S_3/ITO, (c) Au NPs/Bi_2S_3/ITO, (d) BAGs/Au NPs/Bi_2S_3/ITO, (e) SA/BAGs/Au NPs/Bi_2S_3/ITO, (f) BAGs-Au@PCN-224/SA/MBAs/Au NPs/Bi_2S_3/ITO in 5.0 mmol/L $Fe[(CN)_6]^{3-/4-}$ (containing 1.0 mol/L KCl, 0.8 mmol/L TMB and 1.0 mmol/L Ce^{3+}) in the frequency range from 0.01 Hz to 100 KHz at Circuit potential. (B) PEC responses of ITO, Bi_2S_3/ITO, Au NPs/Bi_2S_3/ITO, BAGs/Au NPs/Bi_2S_3/ITO, SA/BAGs/Au NPs/Bi_2S_3/ITO, BAGs-Au@PCN-224/SA/MBAs/Au NPs/Bi_2S_3/ITO (from a to f) in 0.1 mol/L buffer solution at pH 6.4.

42.17 Ω (curve d), 61.83 Ω (curve e) and 85.27 Ω (curve f), respectively. These EIS results indicated that the designed PEC sensor was satisfactorily fabricated according to Scheme S1 (Supporting information).

The electrochemical behaviors of electrode layers in 0.1 mol/L HAc-NaAc buffer solution (pH 6.4) were studied by photocurrent *I-t* responses. From Fig. 3B, low photocurrent was achieved with the bare electrode (curve a) and pure PCN-224 (Fig. S8 in Supporting information). However, after being modified with Bi_2S_3 and Au NPs stepwise, the resulted electrodes of Bi_2S_3/ITO and Au NPs/Bi_2S_3/ITO displayed obviously enhanced photocurrent responses (curves b and c) due to the excellent photoelectric activity of Bi_2S_3 and Au NPs [43–47]. After immobilizing BAGs on the electrode surface *via* the Au-S bonds, the photocurrent decreased due to the nonconductivity of the organic molecule (curve d). Similarly, with recognizing SA, the photocurrent continuously decreased (curve e). After the Au@PCN-224 was introduced onto the electrode, the photocurrent signal was further decreased (curve f). These results were consistent with the EIS data shown in Fig. 3A. Here, the Au@PCN-224 played multiple roles to produce PEC signal. Firstly, the Au@PCN-224 impeded electrons transport from electron donor to the electrode surface owing to the steric hindrance effect. Secondly, the Au@PCN-224 partially despoiled light energy and electron donors from electrode, leading to the obviously reduced photocurrent.

Under the optimum conditions (Fig. S9 in Supporting information), the analytical performances of the photoelectrode corresponding to various concentrations of the SA was evaluated by recording the photoresponse transient current intensity and the meanwhile naked-eye colorimetry.

As shown in Fig. 4A, with the increase of the SA concentration, the photocurrent decreased gradually. The photocurrent decrement value ΔI ($\Delta I = I_0 - I$, where I_0 and I were the photocurrents intensity without and with SA, respectively) was proportional to the logarithm of SA concentrations in the range of 5–1000 μmol/L (Fig. 4B). The linear calibration equation was determined to be ΔI (μA) = 0.6130lg$C$ − 0.4262 (where C was the concentration of SA, μmol/L) with a correlation coefficient (R^2) of 0.9952. Based on the signal-to-noise ratio of S/N = 3, the limit of detection (LOD) was calculated to be 1.44 μmol/L, which was lower than the previous reports (Table S3 in Supporting information). Meanwhile, the Au@PCN-224 also served as the reporting agent of colorimetric-signal readout. As shown in Fig. 4C, under the irradiating light, the Au@PCN-224 could catalyze TMB to oxTMB, but weak color change was observed. After adding Ce^{3+} to the system, obvious color change was observed from colorless to dark blue. These results indicated that the Au@PCN-224 could act as an excellent reporting agent for colorimetric signal with Ce^{3+} as the mediator [48,49]. The mediator mechanism of Ce^{3+} was investigated in detail. According to the investigated results, under light irradiation, Au@PCN-224 catalyzed oxygen to generate reactive oxygen species (ROS) (Fig. S10 in Supporting information). However, owing to the short lifetime, the ROS only oxidized part TMB around the Au@PCN-224. After Ce^{3+} was introduced to the system, it could be oxidized to Ce^{4+} by the excited-state Au@PCN-224 through energy transfer. The resulting Ce^{4+}, which had a long life, followed by migration to far distance and oxidizing O_2 in the whole system to generate more ROS, therefore highly boosting oxidation efficiency of TMB to oxTMB (Fig. 4D). Some research works have reported that the PCN-224 is PEC active [50,51]. In this study, the addition of Ce^{3+} could not only promote TMB rendering, but also promote electrons of PCN-224 to return to its HOMO orbit, which resulted in a radiative electron hole recombination, leading to the decrease of the photoconversion efficiency and photocurrent accordingly. Therefore the PEC signal decreased after further modification of BAGs-Au@PCN-224 on the electrode. As shown in Fig. 4E, with the increase of the SA concentration, the solution exhibited distinct color change from nearly colorless to bright blue gradually. The apparent color change enabled the naked eye distinction for SA sensing, achieving fast qualitative screening and more accurate insurance. Meanwhile, the UV–vis absorption intensity at

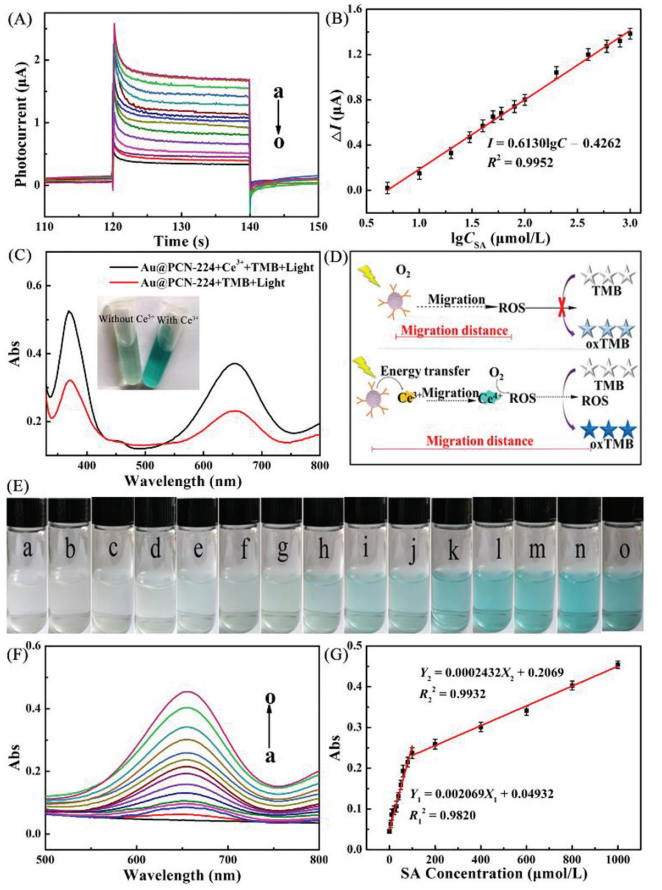

Fig. 4. (A) Photocurrent response of the PEC biosensors with different concentrations of SA: 0, 5, 10, 20, 30, 40, 50, 60, 80, 100, 200, 400, 600, 800, 1000 μmol/L (from a to o). (B) The corresponding calibration curve. (C) UV–vis absorption spectra of Au@PCN-224 photocatalytic TMB in presence and absence of Ce^{3+}. Inset: Photograph of Au@PCN-224 photocatalytic TMB in presence and absence of Ce^{3+}. (D) Schematic illustration of the oxidation of TMB by the Au@PCN-224 without and with Ce^{3+} as the mediator. The mediator could increase the concentration and the effective migration distance of the generated ROS. (E) The photographs of Au@PCN-224 photocatalytic TMB system with SA at different concentrations (consistent with those in A). (F) The UV–vis spectrum response of SA at the different concentrations and (G) the consistent corresponding calibration curve (consistent with those in A and E).

652 nm was also recorded. As shown in Fig. 4F, with the increase of SA concentration, the UV–vis intensity gradually increased (from a to o). The linearity between the UV–vis intensity and the SA concentration was shown in Fig. 4G, and the linear calibration equations were determined to be $Y_1 = 0.002069X_1 + 0.04932$ and $Y_2 = 0.0002432X_2 + 0.2069$ in the ranges of 0–100 μmol/L and 100–1000 μmol/L ($R^2 = 0.9820$ and 0.9932), respectively. Above results showed good linearity during the PEC sensing range.

To evaluate the practicability of the PEC sensing mode, the stability and reproducibility of the PEC mode were explored. The time based photocurrent response of the electrode was measured at "on-off-on" mode for 400 s. As shown in Fig. 5A, negligible photocurrent decline was observed after 9 recycles, indicating the good photocurrent report stability of the PEC mode sensing. The reproducibility of a sensing system was assessed by measuring five independently manufactured biosensors. The photocurrent offered a relative standard deviation (RSD) of 2.49% for 200 μmol/L SA, indicating a satisfactory reproducibility (Fig. S11 in Supporting information).

To investigate the selectivity of the proposed sensor, experiments were carried out by evaluating the dual readout of pho-

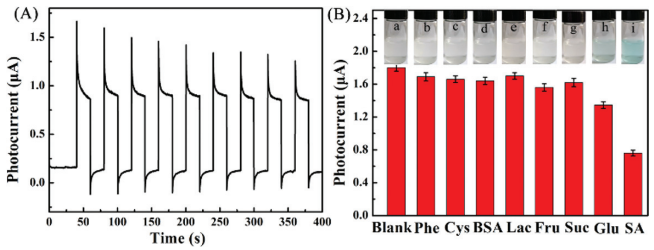

Fig. 5. (A) Stability of the PEC biosensor under several on/off irradiation cycles for 400 s, $C_{SA} = 200$ μmol/L. (B) Selectivity of fabricated biosensor incubated with Blank, Phe, Cys, BSA, Lac, Fru, Suc, Glu (400 μmol/L) and SA (200 μmol/L). Inset: Photographs of the TMB system corresponding to the above substances.

tocurrent and colorimetry under the same experiment conditions by incubating with blank, L-phenylalanine (Phe), L-cysteine (Cys), bovine serum albumin (BSA), lactose (Lac), fructose (Fru), sucrose (Suc), glucose (Glu) and SA. As shown in Fig. 5B, by comparison with the photocurrent response of the blank test, the interference species showed no obvious change on both photocurrent and visual signals. However, after adding SA even with half concentration of interference to the tested solutions, obvious changes were observed. Benefiting from the double *cis*-diol of SA and the analogous immune sandwich assembling, the proposed colorimetric-assisted PEC sensor exhibited high selectivity to SA.

In order to evaluate the analytical reliability and potential applications of the fabricated biosensor for SA in real samples, recovery experiments were performed with spiked serum samples. Three diluted healthy human serum samples (100 times) spiked with different concentrations of SA (200, 500 and 1000 μmol/L) were investigated using the developed method and the results are shown in Fig. S12 and Table S4 (Supporting information). The recoveries were in range of 98.0%−100.8% and the RSD ($n = 3$) were calculated to be less than 3%. These results indicated that the developed biosensor had a good practicability and potential application for the detection of SA in serum samples with great accuracy and reliability.

In summary, this work presented a colorimetric-assisted PEC sensor for sensitive and accurate detection of SA. Thanks to the unique structure of SA, which endowed high specific responding sites to form the sandwich structure with high affinity. With the specific recognition of SA, the Au@PCN-224 was introduced to the electrode as a multiple signal reporter, producing photocurrent signal from on to off and colorimetric signal from off to on with the presence of TMB. Moreover, the participation of Ce^{3+} obviously enhanced the colorimetric signal in the whole system. Therefore, with the assistance of the colorimetric signal and the help of Ce^{3+} as mediator, the developed PEC sensor showed high sensitivity, selectivity and accuracy for SA detection. This method provided a new promising platform for SA detection and a potential strategy for design of novel biosensors with dual-mode readout.

Declaration of competing interest

The authors declare no conflict of interest.

Acknowledgments

This work was supported by grants awarded by the National Natural Science Foundation of China (Nos. 22174086, 21775089 and 22074080), Changjiang Scholar Program of the Ministry of Education of China (No. Q2019258), Natural Science Foundation of Shandong Province (Nos. ZR2020MB056 and ZR2020KB020), Taishan Scholar Program of Shandong Province (No. tsqn201909106), and College Students Innovation and Entrepreneurship Training Project of Shandong Province (No. S201910446019).

References

[1] A. Varki, Nature 446 (2017) 1023–1029.
[2] X.D. Wang, Y.J. Liu, F.J. Li, Z.L. Li, Chin. Chem. Lett. 28 (2017) 1018–1026.
[3] C. Bull, M.A. Stoel, M.H. den Brok, G.J. Adema, Cancer Res. 74 (2014) 3199–3204.
[4] R. Schauer, J.P. Kamerling, Adv. Carbohydr. Chem. Biochem. 75 (2018) 1–213.
[5] A. Matsumoto, N. Sato, K. Kataoka, Y. Miyahara, J. Am. Chem. Soc. 131 (2009) 12022–12023.
[6] T. Miyazaki, T. Khan, Y. Tachihara, et al., ACS Appl. Bio. Mater. 4 (2021) 6647–6651.
[7] Y.Y. Zhou, T.S. Mamie Lih, G.L. Yang, et al., Anal. Chem. 92 (2020) 1842–1849.
[8] K. Miyazaki, K. Ohmori, M. Izawa, et al., Cancer. Res. 64 (2004) 4498–4505.
[9] B. Demir, M.M. Lemberger, M.M. Panagiotopoulou, et al., ACS Appl. Mater. Interfaces 10 (2018) 3305–3313.
[10] T. Li, Y. Liu, Anal. Chem. 93 (2021) 7029–7036.
[11] X.M. Zhou, S. Yang, G.L. Yang, et al., Chin. Chem. Lett. 30 (2019) 676–680.
[12] A.C. Chatziioannou, E. Benjamins, L. Pellis, et al., J. Agric. Food. Chem. 69 (2021) 7851–7862.
[13] C. Büll, T. Heise, N.V. Hilten, et al., Angew. Chem. Int. Ed. 56 (2017) 3309–3313.
[14] L.Y. Liu, S.Y. Zhu, J. Sun, et al., Chin. Chem. Lett. 32 (2021) 906–909.
[15] D. Yi, N. He, M. Kickstein, et al., Adv. Synth. Catal. 355 (2013) 3597–3612.
[16] S.S. Ding, S.M. Cao, Y.Z. Liu, et al., ACS Sensors 2 (2017) 394–400.
[17] Q.H. Yang, Q. Hao, J.P. Lei, H.X. Ju, Anal. Chem. 90 (2018) 3703–3707.
[18] Y.X. Chu, A.P. Deng, W.J. Wang, J.J. Zhu, Anal. Chem. 91 (2019) 3619–3627.
[19] Q.Z. Han, X. Zhao, N. Na, J. Ouyang, Anal. Chem. 93 (2021) 3486–3492.
[20] L.B. Mao, H. Liu, L.L. Yao, et al., Chem. Eng. J. 429 (2022) 132297.
[21] S.P. Wang, F.F. Wang, C.P. Fu, et al., Anal. Chem. 92 (2020) 7604–7611.
[22] X.Y. Yu, Y.Y. Wang, X.M. Chen, et al., Anal. Chem. 87 (2015) 4237–4244.
[23] Y.X. Lin, Q. Zhou, D.P. Tang, et al., Anal. Chem. 89 (2017) 5637–5645.
[24] J.L. Sun, L. Li, S.G. Ge, et al., ACS Appl. Mater. Interfaces 13 (2021) 3645–3652.
[25] D.W. Feng, Z.Y. Gu, J.R. Li, et al., Angew. Chem. Int. Ed. 51 (2012) 10307–10310.
[26] Y.W. Zhao, Y. Kuang, M. Liu, et al., Chem. Mater. 30 (2018) 7511–7520.
[27] N. Antil, A. Kumar, N. Akhtar, et al., Inorg. Chem. 60 (2021) 9029–9039.
[28] C.Q. Cui, G.D. Li, Z.Y. Tang, Chin. Chem. Lett. 32 (2021) 3307–3321.
[29] E.M. Johnson, S. Ilic, A.J. Morris, ACS Cent. Sci. 7 (2021) 445–453.
[30] A. Morozan, F. Jaouen, Energy Environ. Sci. 5 (2012) 9269–9929.
[31] C. Ye, M.Q. Wang, Z.F. Gao, et al., Anal. Chem. 88 (2016) 11444–11449.
[32] C.Y. Hong, Y. Kim, J.H. Seo, et al., ACS Appl. Mater. Interfaces 12 (2020) 39713–39719.
[33] Y.D. Wang, W. Tian, L. Chen, et al., ACS Appl. Mater. Interfaces 9 (2017) 40235–40243.
[34] X. Wang, C.Y. Zhang, J.F. Du, et al., ACS Nano 13 (2019) 5947–5958.
[35] A. Di Pasquale, S. Tommasone, L.L. Xu, et al., J. Org. Chem. 85 (2020) 8330–8338.
[36] H. Otsuka, E. Uchimura, H. Koshino, et al., J. Am. Chem. Soc. 125 (2003) 3493–3502.
[37] R. Sharma, U. Haldar, H.-i. Lee, ACS Sustainable Chem. Eng. 9 (2021) 9915–9922.
[38] S.T. Li, Y.R. Qin, G.Q. Zhong, et al., ACS Appl. Mater. Interfaces 10 (2018) 27612–27620.
[39] D.W. Qi, H.Y. Zhang, J. Tang, et al., J. Phys. Chem. C 114 (2010) 9221–9226.
[40] Z.M. He, X.L. Huang, C. Wang, et al., Angew. Chem. Int. Ed. 58 (2019) 8752–8756.
[41] K. Wang, N.L. Rangel, S. Kundu, et al., J. Am. Chem. Soc. 131 (2009) 10447–10451.
[42] G.J. Yang, Y.X. Lai, Z.Q. Xiao, et al., Chin. Chem. Lett. 29 (2018) 1857–1860.
[43] J.F. Li, L. Liu, Y.J. Ai, et al., ACS Appl. Mater. Interfaces 12 (2020) 5500–5510.
[44] K.C.L. Black, Z.Q. Liu, P.B. Messersmith, Chem. Mater. 23 (2011) 1130–1135.
[45] J.F. Zeng, W.D. Yang, D.J. Shi, et al., ACS Biomater. Sci. Eng. 4 (2018) 963–972.
[46] R. Li, C.C. Zhang, D. Wang, et al., Chin. Chem. Lett. 32 (2021) 2846–2850.
[47] H.W. Lu, Y. Qu, L.Q. Sun, et al., ACS Sustainable Chem. Eng. 6 (2018) 14652–14659.
[48] J.Y. Zhang, S.H. Wu, X.M. Lu, P. Wu, J.W. Liu, Nano Lett. 19 (2019) 3214–3220.
[49] J.Y. Zhang, S.H. Wu, X.M. Lu, P. Wu, J.W. Liu, ACS Nano 13 (2019) 14152–14161.
[50] K.Y. Chen, J.Y. Xue, Q. Zhou, et al., Anal. Chim. Acta 1107 (2020) 145–154.
[51] Q. Zhou, G.H. Li, K.Y. Chen, et al., Anal. Chem. 92 (2020) 983–990.